# Distinct charge density wave instabilities in PrTe$_n$ ($n = 2, 3$) and ErTe$_3$ investigated via ARPES and XAS

J.-S. Kang [1,*] Seungho Seong [1], Eunsook Lee,[1] Y. S. Kwon,[2] Kyoo Kim,[3] Junwon Kim,[4,†]
Heejung Kim,[4,‡] and B. I. Min [4]

[1]*Department of Physics, The Catholic University of Korea, Bucheon 14662, Republic of Korea*
[2]*Department of Physics and Chemistry, DGIST, Daegu 42988, Republic of Korea*
[3]*Korea Atomic Energy Research Institute (KAERI), Daejeon 34057, Republic of Korea*
[4]*Department of Physics, Pohang University of Science and Technology (POSTECH), Pohang 37673, Republic of Korea*

Understanding the origin of distinct charge density wave (CDW) instabilities in layered RTe$_n$ ($n = 2, 3$) compounds (R, rare earth element) has been an important issue. In this research update, we have investigated the electronic structures of PrTe$_n$ ($n = 2, 3$) and ErTe$_3$ layered CDW compounds employing angle-resolved photoemission spectroscopy (ARPES) and soft x-ray absorption spectroscopy (XAS). The trivalent valency of R^{3+} ions is confirmed for PrTe$_n$ ($n = 2, 3$) and ErTe$_3$, supporting that R-Te slabs serve as charge reservoirs and that the CDW instability occurs in the partially filled Te sheets. Both R $4d \rightarrow 4f$ resonant photoemission spectroscopy and photon-energy map measurements provide evidence that R $4f$ electrons do not contribute directly to the CDW formation but that the indirect contribution from Pr $4f$ electrons through the Pr $4f-$Te $5p$ hybridization is feasible in PrTe$_n$ ($n = 2, 3$). Circular and linear dichroism ARPES measurements indicate that the chirality of the Te $5p$ orbitals certainly plays a role in the CDW formation of RTe$_3$ ($R =$ Pr, Er) while it is relatively weak in PrTe$_2$, and that the E_F-crossing orbitals, responsible for the CDW formation, are ordered in plane (in the ac plane) in all of them. Different CDW-induced Fermi surface reconstructions between RTe$_3$ and RTe$_2$ are due to (i) the existence of two Te sheets and one Te sheet per unit cell in RTe$_3$ and RTe$_2$, respectively, so as to produce different numbers of hole carriers, and (ii) the different lattice parameters of Te sheets in RTe$_n$, leading to the different densities of states at E_F.

I. INTRODUCTION

Charge density wave (CDW) transitions, often observed in low-dimensional systems, are widely considered to arise from the Fermi surface (FS) instability [1–4]. Among the extensively studied CDW compounds, layered rare-earth (R) tellurides of RTe$_n$ type ($n = 2, 3$) have attracted much attention [5–8] because they exhibit not only CDW states but also superconductivity (SC) and other emergent quantum critical phenomena [9]. RTe$_n$ has a layered structure, consisting of R-Te slabs separated by square Te sheets. Tellurium sheets are bonded weakly by van der Waals (vdW) interactions (see Fig. 1).

MX_2-type transition-metal dichalcogenides (TMDs) ($M = 3d$, $4d$, $5d$ transition-metal ions; $X =$ S, Se, Te) are well-known CDW materials [11–14]. In MX_2-type TMDs, M d electrons, which are involved in the CDW instabilities, have rather strong on-site Coulomb interactions (U) due to their localized nature. In contrast, Te $5p$ electrons in RTe$_n$, which

are responsible for the CDW instabilities, have smaller U due to their delocalized nature, and so the electronic structures of RTe$_n$ are relatively simpler for the analysis of CDW instabilities than those of MX_2-type TMDs. An interesting feature in RTe$_3$ is double CDW transitions for heavy R elements and a single CDW transition for light R elements [7,15–17]. In contrast, only a single CDW transition is observed for all RTe$_2$ [4,18,19].

Despite extensive studies on the electronic structures of RTe$_n$ ($n = 2, 3$) [15–17,20–28], the mechanism of the CDW deformation in RTe$_3$ is still controversial. Angle-resolved photoemission spectroscopy (ARPES) is a very powerful tool for studying the electronic structures of CDW compounds [14]. ARPES studies of several RTe$_3$ compounds [15–17,20–23] lead to the FS nesting mechanism for the CDW instability. On the other hand, inelastic x-ray scattering and Raman scattering experiments showed that the momentum-dependent electron-phonon coupling is an important mechanism for the CDW formation in RTe$_3$ [29–31]. Curiously, the origin of distinct CDW instabilities in RTe$_n$ between $n = 2$ and $n = 3$ have not been investigated systematically. Further, the role of R $4f$ electrons has been explored only in a few works [24,25,32,33].

To clarify these issues, we have investigated the electronic structures of PrTe$_n$ ($n = 2, 3$) and ErTe$_3$ employing ARPES and soft x-ray absorption spectroscopy (XAS) in this research

---

*Contact author: kangjs@catholic.ac.kr

†Present address: Department of Chemistry, POSTECH, Pohang 37673, Republic of Korea.

‡Present address: MPPHC-CPM, Max Planck POSTECH/Korea Research Initiative, Pohang 37673, Republic of Korea.
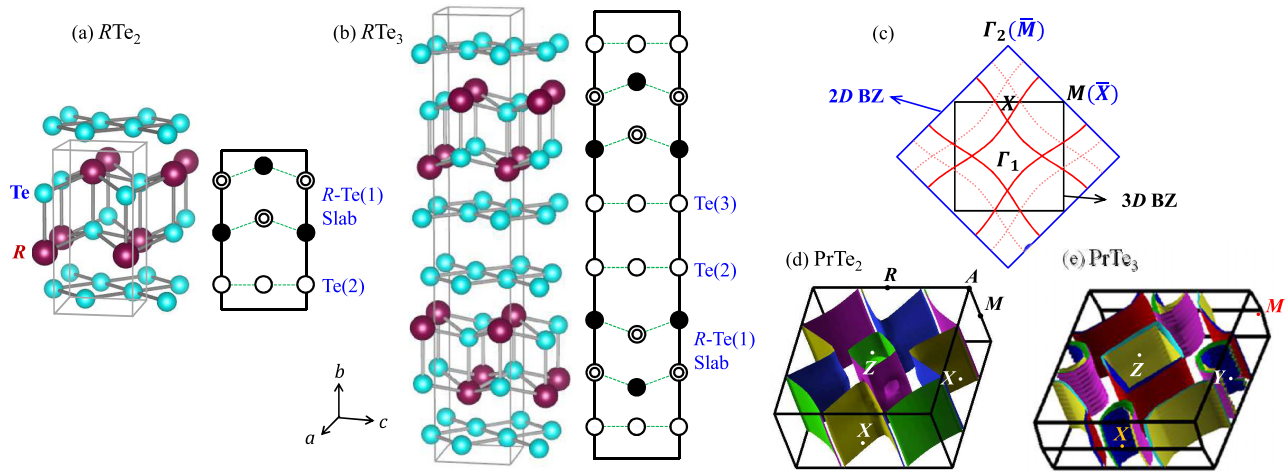
FIG. 1. Crystal structures and Fermi surfaces of $R\mathrm{Te}_2$ and $R\mathrm{Te}_3$. (a) Slightly distorted tetragonal (orthorhombic) crystal structure of $R\mathrm{Te}_2$ (left) and its schematic cross section along the b axis (right). (b) Similarly for $R\mathrm{Te}_3$. (c) A sketch of the two-dimensional (2D) Fermi surface (FS) of $R\mathrm{Te}_2$ in the non-CDW phase (solid red line) on the 2D Brillouin zone (BZ) of the Te sheet (blue). Shadow FS in dotted red line corresponds to the 2D FS folded into the reduced three-dimensional (3D) BZ of $R\mathrm{Te}_2$ (black). [(d), (e)] The calculated 3D FSs of PrTe_2 and PrTe_3, respectively, in their non-CDW phases. Γ, X, M, and Z symmetry points in (d) correspond to $\vec{k} = (0, 0, 0)$, $(\frac{\pi}{a}, 0, 0)$, $(\frac{\pi}{a}, \frac{\pi}{a}, 0)$, and $(0, 0, \frac{\pi}{b})$, respectively. In (e), the Y symmetry point corresponds to $(0, \frac{\pi}{c}, 0)$ while X and M that are not symmetry points of the orthorhombic BZ are considered here just for the comparison with those for PrTe_2 [10].

update. $R = \mathrm{Pr}$ $(Z = 59)$ and $R = \mathrm{Er}$ $(Z = 68)$ belong to a light and heavy $R\mathrm{Te}_3$, respectively. ErTe_3 has two well-separated CDW transitions at $T_{\mathrm{CDW1}} = 267$ K and $T_{\mathrm{CDW2}} = 157$ K [7,9,15–17] while PrTe_3 is presumed to have only one CDW transition at higher than 450 K $(T_{\mathrm{CDW}} > 450$ K) [7,9,34]. T_{CDW} of PrTe_2 is expected to be $T_{\mathrm{CDW}} \sim 1000$ K [35] (see Table I).

II. EXPERIMENTAL DETAILS

High-quality single crystals of $R\mathrm{Te}_n$ $(R = \mathrm{Pr}, \mathrm{Er}; n = 2, 3)$ were grown by using the self-flux Bridgeman method [24]. The quality and the orientation of single crystals were checked by Laue and ARPES measurements. The long axis, perpendicular to the layers, is conventionally taken as the c axis in $R\mathrm{Te}_2$ while it is the b axis in $R\mathrm{Te}_3$ [39]. In order to compare $R\mathrm{Te}_2$ and $R\mathrm{Te}_3$, we have chosen the long axis as b for both $R\mathrm{Te}_2$ and $R\mathrm{Te}_3$ in this work (see Fig. 1). The lattice parameters of a and c in the ac planes are very similar to each other while b is much larger than a and c [36–38,40]. The lattice parameters and the T'_{CDW} values are listed in Table I.

ARPES measurements were carried out at the 4A2 undulator beamline of the Pohang Light Source-II (PLS-II) and

the 4.0.3 undulator beamline of the Advanced Light Source (ALS). Single crystalline samples were cleaved *in situ* by using the top-post method and measured under pressure better than 5×10^{-11} Torr. The Fermi level (E_{F}) and the instrumental resolution of the system were determined from the Fermi edge spectrum of the Au metal in electrical contact with samples. The energy resolution of the ARPES data is set to be ~30 meV. The details of ARPES experiments are described in Refs. [24,25].

III. CRYSTAL STRUCTURE, TWO- AND THREE-DIMENSIONAL BRILLOUIN ZONES, AND FERMI SURFACES

Figures 1(a) and 1(b) show the quasi-2D layered orthorhombic (slightly distorted from tetragonal) structures of $R\mathrm{Te}_n$ $(n = 2, 3)$ with their schematic cross sections along the b axis. R-Te(1) slabs are common for $n = 2$ and 3, where Te(1) and R atoms form the corrugated double layers. $R\mathrm{Te}_2$ has single Te(2) planar sheets and $R\mathrm{Te}_3$ has Te(2)/Te(3) bilayer planar sheets, sandwiched between R-Te(1) slabs along the b axis [18,19].

Figure 1(c) shows the 2D Brillouin zone (BZ) (blue lines), the 3D BZ (black lines), and the schematic FS of $R\mathrm{Te}_2$ in the non-CDW phase. Due to the R-Te(1) slabs, the unit cell (u.c.) of the 3D orthorhombic structure is doubled by $\sqrt{2} \times \sqrt{2}$ and rotated by 45° from the 2D u.c. of the planar Te sheets. Such an enlarged 3D u.c. yields a reduced 3D BZ; i.e., the size of the 3D BZ is decreased by half and rotated by 45° from the 2D BZ of the planar Te sheets. When the FS in the 2D BZ is folded into the reduced 3D BZ, the folded shadow FS (dotted red lines) appears in the 3D BZ. Consequently, the intensity of the inner (smaller) FS around the Γ point (solid red line) is stronger than that of the outer (larger) shadow FS (dotted red line). The stronger the interlayer interaction between the Te sheets and the R-Te(1) slabs is, the higher the

TABLE I. Lattice parameters a, b, and c, and the CDW transition temperatures T_{CDW1} and T_{CDW2} of $R\mathrm{Te}_n$ $(R = \mathrm{Pr}, \mathrm{Er}; n = 2, 3)$. For the in-plane lattice parameters, the same values are adopted for a and c because of the very subtle difference between them (c is slightly larger than a in $R\mathrm{Te}_3$).

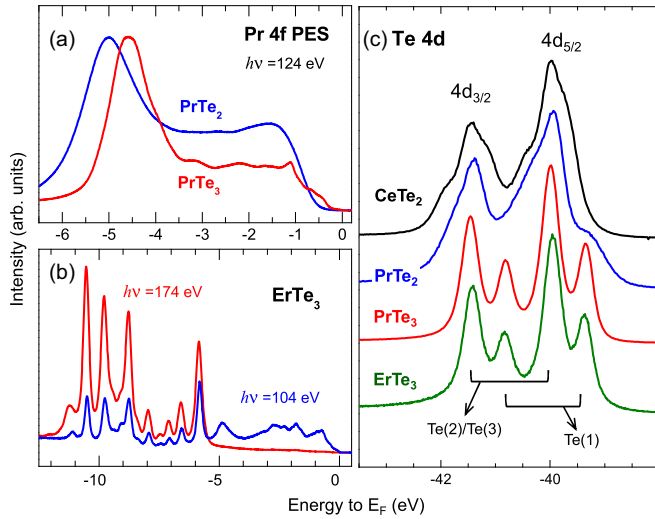| Materials	$a \approx c$	b	T_{CDW1}	T_{CDW2}
PrTe_2 [36]	4.44 Å	9.06 Å	~1000 K [35]	
PrTe_3 [37]	4.36 Å	25.89 Å	>450 K [34]	
ErTe_3 [38]	4.29 Å	25.30 Å	267 K [7]	157 K [7]

FIG. 2. Core-level and $R\,4f$ photoemission spectroscopy (PES) spectra of $R\mathrm{Te}_n$ (R = Pr, Er; n = 2, 3). (a) Comparison of the angle-integrated Pr $4f$ PES spectra of PrTe_2 and PrTe_3, obtained at the on-resonance energy ($h\nu = 124$ eV) in Pr $4d \rightarrow 4f$ resonant photoemission spectroscopy (RPES). (b) Comparison of the angle-integrated valence-band PES spectra of ErTe_3, obtained at the on-resonance energy ($h\nu = 174$ eV) and far away from the resonance ($h\nu = 104$ eV) in Er $4d \rightarrow 4f$ RPES, respectively. (c) Comparison of the Te $4d$ core-level PES spectra of $R\mathrm{Te}_n$ (R = Pr, Er; n = 2, 3), obtained at $h\nu \approx 100$ eV. The data of PrTe_2 and PrTe_3 were obtained at $T \approx 35$ K and those of ErTe_3 were obtained at $T \approx 80$ K.

intensity of shadow FSs becomes, accompanied by a larger FS dispersion along k_b due to the 3D-like nature.

Figures 1(d) and 1(e) show the calculated 3D FSs of the non-CDW phases of PrTe_2 and PrTe_3, respectively. The shapes of the 3D FSs of PrTe_2 and PrTe_3 are similar to each other, supporting the fact that the FSs of both PrTe_2 and PrTe_3 are determined mainly by the Te $5p$ electrons of Te sheets. On the other hand, the size of the inner FS centered at Γ or Z points in PrTe_3 is larger than that in PrTe_2. Such differences suggest that the inner FS centered at Γ or Z arises from the hole pocket, supported by the trivalent (3+) nature of R ions (as explained below).

If R ions are trivalent (3+) and donate two electrons to R-Te(1) slabs and one electron to Te sheets, then the ionic configuration of $R\mathrm{Te}_2$ will be $R^{3+}\mathrm{Te}(1)\,^6\mathrm{Te}(2)^5$ [27] with a partially filled Te sheet while that of $R\mathrm{Te}_3$ will be $R^{3+}\mathrm{Te}(1)\,^6\mathrm{Te}(2)^{4.5}\mathrm{Te}(3)^{4.5}$ with two partially filled Te sheets. These configurations will be confirmed in Sec. IV. Thus, more hole carriers are produced in $R\mathrm{Te}_3$ (1.5 holes per Te sheet) than in $R\mathrm{Te}_2$ (1 hole per Te sheet), yielding a larger hole FS in $R\mathrm{Te}_3$ than in $R\mathrm{Te}_2$.

IV. $R\,4f$ STATES

Figure 2(a) compares the angle-integrated Pr $4f$ PES spectra of PrTe_n (n = 2, 3), obtained at the on-resonance energy ($h\nu = 124$ eV; $h\nu$, photon energy) in Pr $4d \rightarrow 4f$ resonant photoemission spectroscopy (RPES). Similarly, Fig. 2(b) compares the angle-integrated valence-band PES spectra of

ErTe_3, obtained at the on-resonance energy ($h\nu = 174$ eV) and far away from the resonance ($h\nu = 104$ eV) in Er $4d \rightarrow 4f$ RPES, respectively. All the data were obtained in their CDW phases (at $T \approx 35$ K for PrTe_2 and PrTe_3, and at $T \approx 80$ K for ErTe_3).

The peaks that exhibit strong resonance enhancement in the on-resonance spectra represent $R\,4f$ states, arising from the well-known $R\,4d \rightarrow 4f$ resonance [41]. In PrTe_2 and PrTe_3, the Pr $4f$ peaks well below E_F (~ -4 eV) represent the trivalent Pr $4f^2 \rightarrow 4f^1$ transition. Similarly, the Er $4f$ peaks between -5 and -12 eV in ErTe_3 correspond to the $4f^{10}$ final-state multiplets from the $\mathrm{Er}^{3+}\,4f^{11} \rightarrow 4f^{10}$ transition. Such Er $4f$ multiplets in ErTe_3 are similar to those in other Er materials [42,43]. In both R = Pr and Er, the bare $R\,4f^{n-1}$ final-state multiplets are located well below E_F, indicating that $R\,4f$ electrons are very localized for both R = Pr and Er. Considering that the metallic electronic states near E_F are important to cause the CDW instabilities, the very localized character of $R\,4f$ electrons manifests the weak contribution of $R\,4f$ electrons to the CDW formation.

Note that the low-energy Pr $4f$ peaks (at ~ -1 eV) correspond to the $4f^2\bar{L}$ final states ($4f^2 \rightarrow 4f^2\bar{L}$) (where $\bar{L}$ is a ligand hole in Te $5p$ bands) arising from the Pr $4f$–Te $5p$ hybridization [41,44,45]. In contrast to the significantly large Pr $4f$ spectral weight at ~ -1 eV in PrTe_n (n = 2, 3), the Er $4f$ spectral weight of the $4f^{11} \rightarrow 4f^{11}\bar{L}$ peak near E_F is negligibly weak in ErTe_3. Such differences in $R\,4f$ spectral weight near E_F between R = Pr and R = Er indicate that the Pr $4f$–Te $5p$ hybridization is much larger than the Er $4f$–Te $5p$ hybridization. Compared to the R elements with small Z (where Z is the atomic number), the $R\,4f$ electrons in the R elements with large Z are located at deep binding energies because of the strong attractive Coulomb interaction between heavy R ions and $4f$ electrons. Consequently, the localized $R\,4f$ states are located well below the Te $5p$ states in heavy $R\mathrm{Te}_n$ while the less-bound $R\,4f$ states in light $R\mathrm{Te}_n$ overlap with the Te $5p$ states, resulting in the weaker $R\,4f$–Te $5p$ hybridization in heavy $R\mathrm{Te}_n$ than in light $R\mathrm{Te}_n$. Therefore, the Pr $4f$ electrons in PrTe_n would possibly contribute to the CDW formation indirectly through the Pr $4f$–Te $5p$ hybridization while the Er $4f$ electrons would hardly contribute to the CDW formation.

Finally, differences are observed in the Pr $4f$ spectra of PrTe_2 and PrTe_3:

(i) The bare Pr^{3+} peak ($4f^2 \rightarrow 4f^1$) in PrTe_3 (~ -4.5 eV) is located closer to E_F than that in PrTe_2 (~ -5 eV), suggesting the stronger Pr $4f$–Te $5p$ hybridization in PrTe_3 than in PrTe_2.

(ii) In the $4f^2\bar{L}$ final-state peaks, the Pr $4f$ spectral intensity near E_F is finite in PrTe_3 while it is very weak in PrTe_2, in agreement with the more metallic resistivity in PrTe_3 than in PrTe_2.

These differences indicate that the contribution from Pr $4f$ electrons to the CDW formation through the Pr $4f$–Te $5p$ hybridization is larger in PrTe_3 than in PrTe_2. This conclusion is supported by the findings of Fig. 5 below.

Figure 2(c) shows the Te $4d$ core-level PES spectra of $R\mathrm{Te}_2$ (R = Ce, Pr) and $R\mathrm{Te}_3$ (R = Pr, Er). Te $4d$ core levels exhibit $4d_{5/2}$ and $4d_{3/2}$ components, separated by the spin-orbit (SO) splitting, where each SO component consists of
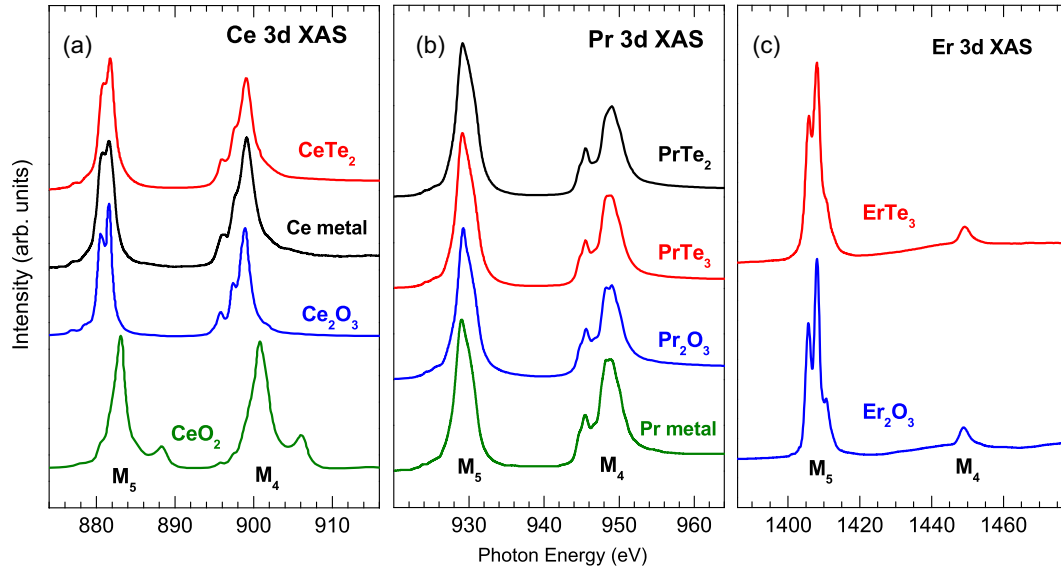
FIG. 3. R $3d$ XAS spectra of RTe$_n$ (R = Ce, Pr, Er; n = 2, 3). (a) The Ce $3d$ XAS spectrum of CeTe$_2$, in comparison to those of Ce metal, trivalent Ce$_2$O$_3$, and tetravalent CeO$_2$. (b) The Pr $3d$ XAS spectra of PrTe$_2$ and PrTe$_3$, in comparison to those of trivalent Pr$_2$O$_3$ and Pr metal. (c) The Er $3d$ XAS spectrum of ErTe$_3$, compared to that of trivalent Er$_2$O$_3$. All the R $3d$ XAS spectra were obtained at $T \approx 80$ K.

multiple peaks. The similarity between Pr and Er in RTe$_3$ and that between Ce and Pr in RTe$_2$ reveal that these Te $4d$ core-level PES spectra represent the intrinsic features of RTe$_n$. Multiple peaks are expected to arise from two different Te sites [25], one at R-Te(1) slabs [low-binding-energy (BE) peaks] and the other at Te(2)/Te(3) sheets (high-BE peaks), respectively, which is confirmed by the calculated BE values [46]. The Te $4d$ core-level line shapes of RTe$_2$ are more complicated than those of RTe$_3$. The relative weights among the multiple peaks in the core-level PES depend on which cleavage planes are exposed to photons [47]. In reality, however, it is likely that the cleaved surfaces consist of different planes.

Figure 3(a) shows the Ce $3d$ XAS spectrum of CeTe$_2$, in comparison to those of the reference materials, such as Ce metal, trivalent Ce$_2$O$_3$, and tetravalent CeO$_2$. Figure 3(b) shows the Pr $3d$ (M edge) XAS spectra of PrTe$_2$ and PrTe$_3$, in comparison to those of trivalent Pr$_2$O$_3$ and metallic Pr metal. Similarly, Fig. 3(c) shows the Er $3d$ XAS spectrum of ErTe$_3$, in comparison to that of trivalent Er$_2$O$_3$ [48].

The Ce $3d$ XAS spectrum of CeTe$_2$ shows clearly that Ce ions are trivalent, having the ground state ($|g\rangle$) configuration of $|g\rangle \approx |4f^1\rangle$. The Pr $3d$ XAS spectra of both PrTe$_2$ and PrTe$_3$ are very similar to each other and also to that of trivalent (3+) Pr$_2$O$_3$ and Pr metal, indicating that Pr ions are nearly trivalent, with $|g\rangle \approx |4f^2\rangle$. Similarly, Er ions in ErTe$_3$ are found to be trivalent, with $|g\rangle \approx |4f^{11}\rangle$. The findings in Fig. 3 provide evidence that the valence states of R ions in RTe$_n$ are nearly trivalent (R^{3+}) so that each R ion donates three electrons per unit cell. This finding supports the previous consensus (see the discussion in Fig. 1) that the R-Te(1) slabs serve as charge reservoirs and that the CDW instability occurs in the Te(2)/Te(3) sheets. The fully occupied Pr-Te(1) slabs become semiconducting while the partially filled Te(2)/Te(3) sheets become metallic, and easily distorted to form the CDW phase. It was proposed that, due to partial filling, the square

nets of Te sheets are easily distorted by the Peierls-like mechanism [49,50], which was supported by the band-structure calculations [18,19,51–53]. Our finding of trivalent R^{3+} ions satisfies the prerequisite condition of partial filling for the FS nesting mechanism, even though the electron-phonon mechanism is not ruled out either.

V. CONSTANT ENERGY MAPS AND FERMI SURFACES

Figure 4 shows the measured constant energy (CE) maps of PrTe$_2$, PrTe$_3$, and ErTe$_3$ in the momentum space. The labels in Fig. 4 denote the initial-state energies (E_i'), which vary from $E_i = 0$ eV ($= E_F$) to $E_i = -0.8$ eV with decrement by -0.2 eV. Here, the horizontal and vertical directions are along $k_{a(100)}$ and $k_{c(010)}$, respectively. All these CE data were obtained with the linear horizontal (LH) polarization. The CE maps in this figure were made by integrating the spectral intensity of $E_i \pm 16$ meV for each E_i. The overall intensity of each map has been scaled by an arbitrary scale factor.

With decreasing E_i, the shapes and the behavior of the CE maps of RTe$_2$ and RTe$_3$ are similar to one another for $E_i \lesssim \sim -0.4$ eV. Such similarities indicate that the measured CE maps represent those of the Te square nets in the Te(2)/Te(3) sheets. This also implies the weak interlayer interaction and so the weak contribution of R $4f$ electrons to the CDW distortion in RTe$_n$. This finding is consistent with the Peierls-like mechanism of the CDW deformation in RTe$_n$, as described above. However, the shapes of the FSs among PrTe$_2$, PrTe$_3$, and ErTe$_3$ are quite different. The origin of these differences will be discussed in Fig. 5.

Figure 4(d) shows the calculated CE maps for the non-CDW phase of ErTe$_3$ from $E_i = +0.2$ eV to $E_i = -0.6$ eV, which are obtained from the DFT calculations. When the calculated CE maps are sliced at higher E_i' by $\sim +0.2$ eV, the measured and calculated CE maps agree very well [54] [see Figs. 4(c) and 4(d)]. Such a good agreement in ErTe$_3$
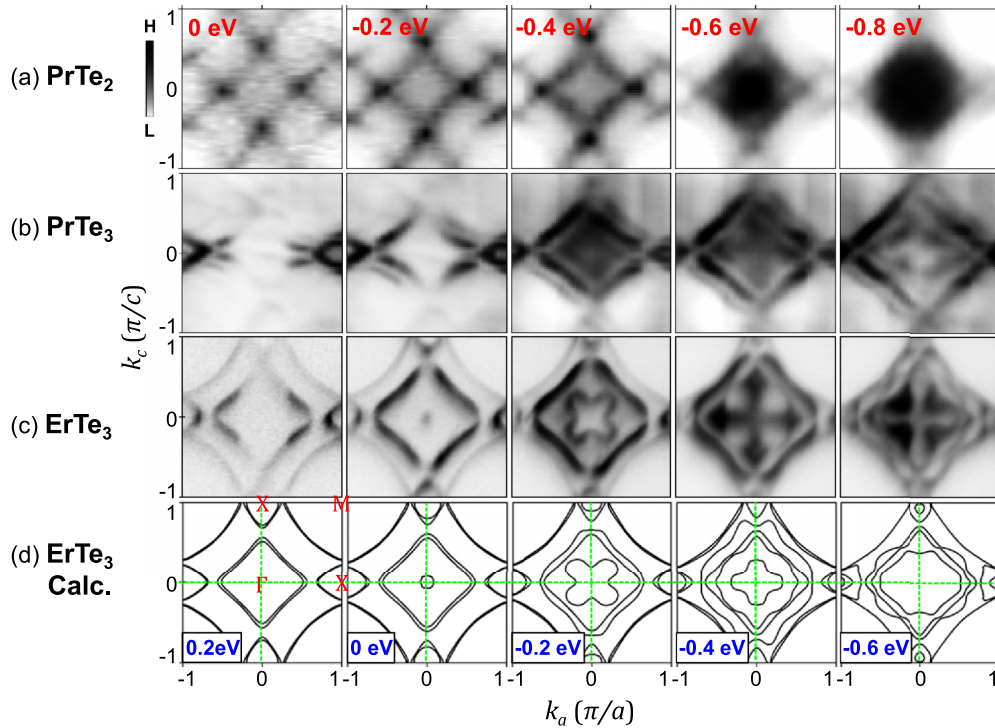
FIG. 4. Comparison of the measured constant energy (CE) maps of $PrTe_2$, $PrTe_3$, and $ErTe_3$. (a) CE maps of $PrTe_2$ on the [001] ($k_b = 0$) plane of $PrTe_2$ in the momentum space. The labels denote the initial-state energies (E_i'), which vary from $E_i = 0$ eV ($= E_F$) to $E_i = -0.8$ eV with decrement by -0.2 eV. Here, the horizontal and vertical directions are along $k_{a(100)}$ and $k_{c(010)}$, respectively. [(b), (c)] Similarly for $PrTe_3$ and $ErTe_3$. These CE data were obtained at $h\nu = 104$ eV with the linear horizontal (LH) polarization, except for $PrTe_2$ that was obtained at $h\nu = 110$ eV. The CE data for $PrTe_2$ and $PrTe_3$ were obtained at $T \approx 35$ K while those for $ErTe_3$ were obtained at $T \approx 80$ K. (d) The calculated CE maps for the non-CDW phase of $ErTe_3$, obtained from the density functional theory (DFT) calculations. In the comparison between experiment and calculations, the calculated maps were shifted by $+0.2$ ev; i.e., the calculated maps were cut at higher E_i by $+0.2$ eV.
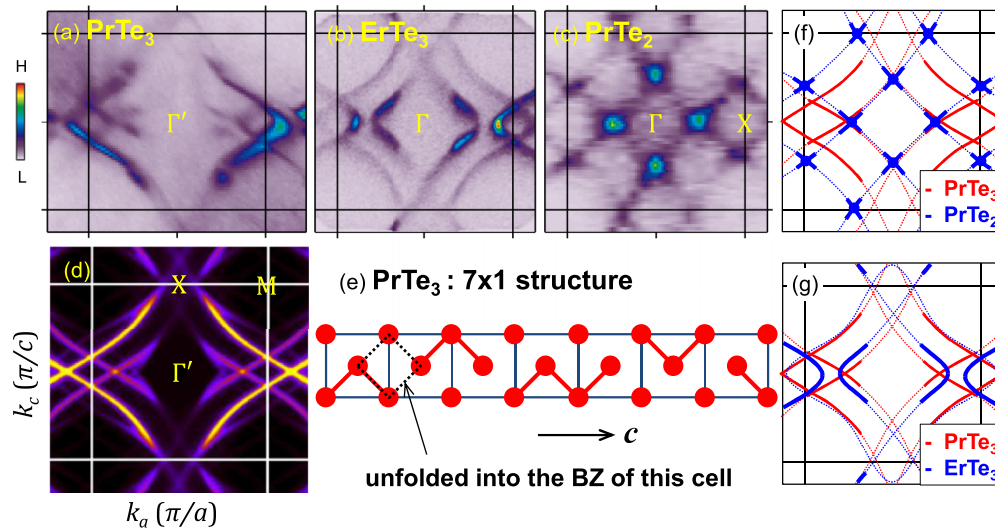

FIG. 5. FSs of $PrTe_3$, $ErTe_3$, and $PrTe_2$ in the CDW phase. [(a)–(c)] The measured FSs of $PrTe_3$, $ErTe_3$, and $PrTe_2$, respectively, which were obtained at $h\nu \approx 104$ eV ($h\nu = 110$ eV for $PrTe_2$) and below their CDW transition temperatures (at $T = 35$ K for $PrTe_2$ and $PrTe_3$; and at $T = 80$ K for $ErTe_3$). (d) The calculated FS of $PrTe_3$ for the 7×1 supercell structure [shown in (e)], which is then unfolded into the 2D BZ. This calculated FS was obtained using the tight-binding (TB) model, and reproduced from Fig. 3 in Ref. [23]. (e) The putative CDW-supercell structure of the 7×1 u.c. in the bilayer Te sheets. The dumbbells, connected via red bars, represent the dimerized Te atoms. Trimers and tetramers serve as the basic building blocks. (f) The schematically drawn FS of $PrTe_3$ (red) in comparison with that of $PrTe_2$ (blue). (g) The schematically drawn FS of $PrTe_3$ (red) in comparison with that of $ErTe_3$ (blue).

supports that the normal-state electronic structures of $R\text{Te}_n$ are described well by the DFT calculations and that the contribution of R $4f$ electrons to the CDW distortion is weak in $R\text{Te}_n$ due to the weak interlayer interaction.

Figures 5(a)–5(c) show the FSs of $PrTe_3$, $ErTe_3$, and $PrTe_2$, respectively, obtained well below their CDW transition temperatures. FS reconstructions under the CDW instabilities are clearly manifested, and the FSs are seen to be only partially gapped. Common and different features are as follows:

(i) The FS of $PrTe_3$ exhibits the most pronounced CDW-distorted features, as compared to $ErTe_3$ and $PrTe_2$. In $PrTe_3$ [Fig. 5(a)], the FS intensity nearly vanishes (gapped) around the vertical X points $(0, \pm\frac{\pi}{c})$ while it is appreciably finite (ungapped) at the horizontal corners of the inner and outer FSs, resulting in the twofold-symmetric FS.

(ii) $ErTe_3$ also exhibits the twofold-symmetric FS, but, distinctly from that in $PrTe_3$, the FS around the vertical X points appears to be not fully gapped. Furthermore, gapping appears at the horizontal corners of the inner FS (i.e., gapping appears along the horizontal $X\Gamma X$ line).

(iii) The reconstructed FS in $PrTe_2$ is fourfold symmetric with weak gapping along the side lines of the diamond-shaped FS but no gapping on the corners of the FS. Also, the overall FS reconstruction appears to be weak as compared to those in $PrTe_3$ and $ErTe_3$.

To understand the origin of the distinct CDW distortions in $R\text{Te}_n$, we have done the TB model calculations for $PrTe_3$. Figure 5(d) shows the TB-calculated FS for the 7×1 supercell structure, which is then unfolded into the 2D BZ. The putative CDW supercell structure of the 7×1 u.c. in the bilayer Te sheets is drawn schematically in Fig. 5(e), where trimers and tetramers serve as the basic building blocks. The dumbbells, connected by red bars, represent the dimerized Te atoms. The good agreement between the measured and calculated FSs of $PrTe_3$ indicates that the 7×1 supercell structure is a good candidate CDW structure for $PrTe_3$. This 7×1 super-cell structure is large enough to take into account the local oligomer-type distortion [37] of the Te(2)/Te(3) atoms in the CDW state. In other words, the CDW state of $PrTe_3$ is locally commensurate within the domains (i.e., "discommensurate") [47], having the CDW wave vector (Q_{CDW}) of $Q_{CDW} \approx \frac{2}{7}c^*$. The comparison between Figs. 5(a) and 5(b) shows that the twofold-symmetric feature of the CDW-induced FS of $ErTe_3$ is similar to (even though weaker than) that of $PrTe_3$, suggesting that Q_{CDW} in $ErTe_3$ is also likely to be $Q_{CDW} \approx \frac{2}{7}c^*$ (or $Q_{CDW} \approx \frac{2}{7}a^*$).

The schematically drawn FSs of $PrTe_2$, $PrTe_3$, and $ErTe_3$ are compared in Figs. 5(f) and 5(g), manifesting that the size and shape of the FS of $PrTe_3$ are very similar to those of $ErTe_3$, but somewhat different from those of $PrTe_2$. The origin of such differences is likely due to (i) the existence of two Te sheets per unit cell in $R\text{Te}_3$ in contrast to one Te sheet per unit cell in $R\text{Te}_2$, and (ii) the different crystal structures between $R\text{Te}_3$ and $R\text{Te}_2$, namely, twofold-symmetric orthorhombic for the former and fourfold-symmetric tetragonal for the latter. In the case of orthorhombic $R\text{Te}_3$, due to the slightly different lattice parameters of a and c ($c > a$), the CDW instability occurs first with Q_{CDW} along the c direction [55], causing the twofold-symmetric FS reconstruction. On the other hand, for tetragonal $R\text{Te}_2$, the CDW instability either along the a or c direction is feasible, realizing the fourfold-symmetric FS reconstruction.

Somewhat different FS features between $PrTe_3$ and $ErTe_3$ and the absence of the second CDW transition in $PrTe_3$ (i.e., a single CDW transition in $PrTe_3$ versus double CDW transitions in $ErTe_3$) are expected to arise from the much larger lattice parameters of Te sheets in $PrTe_3$ than in $ErTe_3$ (see Table I). This leads to the weaker overlap, the narrower bandwidth, and the higher density of states at E_F [$N(E_F)$] in $PrTe_3$ than in $ErTe_3$. Consequently, the larger energy gain is achieved in $PrTe_3$ by the first CDW transition [52]. On the contrary, due to the smaller energy gain by the CDW instability in $ErTe_3$, $N(E_F)$ even after the first CDW transition remains still high enough to drive the second CDW transition in $ErTe_3$ [7]. The higher T_{CDW1} of $PrTe_2$ than that of $PrTe_3$ can be understood based on the higher occupation of p electrons in the one-dimensional Te $5p_x$ and $5p_z$ bands as well as the larger lattice parameters of Te sheets in $PrTe_2$ than in $PrTe_3$. Both effects bring about the higher $N(E_F)$ [52] and a higher T_{CDW1} in $PrTe_2$ than in $PrTe_3$.

VI. CIRCULAR AND LINEAR DICHROISM

The investigation of circular dichroism (CD) in ARPES is very useful because the observed CD reflects the chiral polarizations of the orbital and spin states of the system [56]. In the CDW state, the local symmetry of a system, such as inversion and/or possibly time-reversal symmetry, could be broken so that the band structures would have $\vec{k}$-dependent chiral spin and orbital polarizations. Then the system in the CDW state is expected to exhibit CD effects in CD-ARPES, even though the system is nonmagnetic (i.e., the total spin and/or orbital polarizations are vanishing). Hence the CD-ARPES study of $R\text{Te}_n$ might give a clue to the origin of their distinct CDW instabilities. However, there is a technical problem of distinguishing between the intrinsic and the extrinsic geometrical CD effects in ARPES [57,58]. This makes it difficult to interpret the observed CD in CD-ARPES.
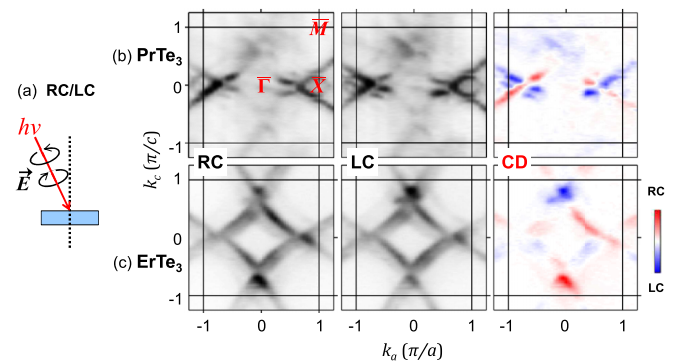

FIG. 6. Circular dichroism (CD) FS of $R\text{Te}_3$ ($R = $ Pr, Er). (a) The schematic drawing of the measurement geometry for the right-circular (RC) and left-circular (LC) polarizations. [(b), (c)] The measured FSs of $PrTe_3$ and $ErTe_3$, respectively, obtained with the RC polarization (left) and LC polarization (middle), and the difference between them (right), corresponding to the CD FS. In the CD FS, red and blue denote stronger RC and stronger LC intensities, respectively. All these data were obtained at $h\nu = 104$ eV and at $T \approx 35$ K.
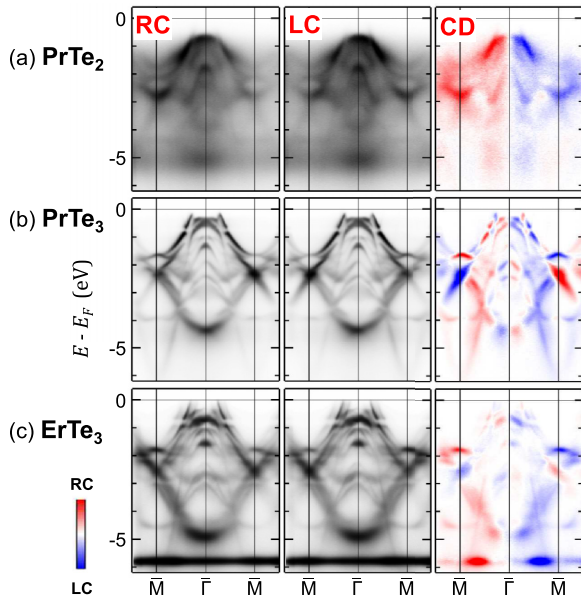
FIG. 7. CD-ARPES of RTe$_n$ ($n = 2, 3$; $R =$ Pr, Er). (a) The measured ARPES image plots of PrTe$_2$ along $\bar{M}\bar{\Gamma}\bar{M}$, obtained with the RC polarization (left) and LC polarization (middle), and the corresponding CD (right) (CD $\equiv$ RC-LC), respectively. [(b), (c)] Similarly for PrTe$_3$ and ErTe$_3$. These ARPES data were obtained at $h\nu = 104$ eV and at $T \approx 35$ K.

Figure 6 shows the measured CD FS of RTe$_3$ ($R =$ Pr, Er). In Fig. 6(a) is shown the schematic drawing of the measurement geometry for the right-circular (RC) and left-circular

(LC) polarizations. In Figs. 6(b) and 6(c) are shown the measured FSs of PrTe$_3$ and ErTe$_3$, respectively, obtained with the RC polarization (left), LC polarization (middle), and the difference between them (right), which corresponds to CD in the FS [59]. In CD FS, red and blue denote stronger RC intensity and stronger LC intensity, respectively. The observed CD effect in the measured CD FSs of RTe$_3$ appears to be weak, but the intrinsic CD is observed clearly in the CD-ARPES data of RTe$_3$, as shown in Fig. 7.

The effects of CD in ARPES of RTe$_n$ ($n = 2, 3$; $R =$ Pr, Er) are shown in Fig. 7. Figure 7(a) shows the measured ARPES image plots of PrTe$_2$ along $\bar{M}\bar{\Gamma}\bar{M}$, obtained with the RC (left) and LC (middle) polarizations, and the corresponding CD $\equiv$ RC-LC (right). Similarly, the measured CD-ARPES for PrTe$_3$ and ErTe$_3$ along $\bar{M}\bar{\Gamma}\bar{M}$ are shown in Figs. 7(b) and 7(c), respectively. In all the measured CD-ARPES of RTe$_n$ ($n = 2, 3$; $R =$ Pr, Er), from E_F near $\bar{\Gamma}$ to ~ -6 eV around $\bar{M}$ exhibit mostly stronger RC for the left side and stronger LC for the right side. These common features indicate that the overall CD effects in the dispersive bands arise from the Te $5p$ states in RTe$_n$. The flat R $4f$ states at ~ -4.5 to ~ -5 eV in PrTe$_n$ and at ~ -6 eV in ErTe$_3$ reveal stronger RC for the left side and stronger LC for the right side, the sign of which is same as that of the above-described dispersive Te $5p$ bands. Such similar signs of CD for both R $4f$ and Te $5p$ states imply that the major contribution to the observed CD in RTe$_n$ is the extrinsic geometric effect.

In a close examination of the CD-ARPES of PrTe$_3$, however, the additional CD effects are observed, as follows. The bands crossing E_F at $\sim \pm \frac{1}{3}\bar{\Gamma}\bar{M}$ exhibit stronger LC for the
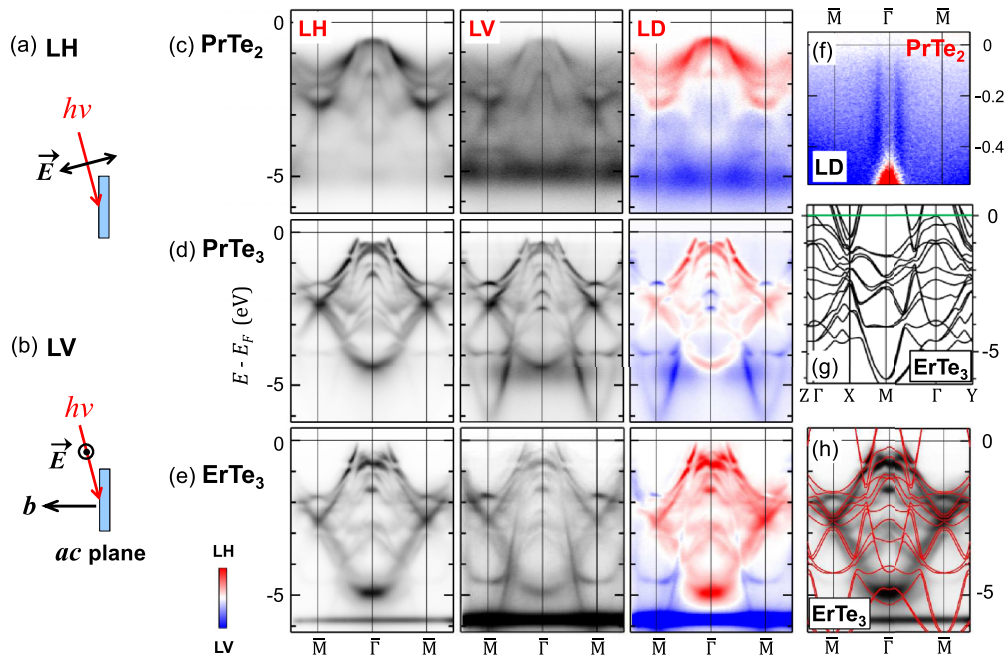

FIG. 8. Linear dichroism (LD) in ARPES. [(a), (b)] The schematic drawings of the measurement geometry for the linear-horizontal (LH) polarization and linear-vertical (LV) polarization, respectively. (c) From left to right, the measured ARPES image plots of PrTe$_2$ along $\bar{M}\bar{\Gamma}\bar{M}$, obtained with the LH and LV polarizations, and LD-ARPES (LD $\equiv$ LH-LV), respectively. In LD-ARPES, red and blue represent the stronger LH and LV intensities, respectively. [(d), (e)] Similarly for PrTe$_3$ and ErTe$_3$, respectively. All these data were obtained at $h\nu = 104$ eV and $T \approx 35$ K. (f) The near-E_F region of the LD-ARPES image plot of PrTe$_2$ along $\bar{M}\bar{\Gamma}\bar{M}$. (g) The calculated band structures of ErTe$_3$ along several high-symmetry lines, obtained from DFT calculations for the non-CDW phase (undistorted phase). (h) Comparison between ARPES and the calculated band structures of ErTe$_3$ along $\bar{M}\bar{\Gamma}\bar{M}$.

left side and stronger RC for the right side, the sign of which is opposite to that of the overall geometrical CD in the steeply dispersive Te $5p$ bands and the flat $R\,4f$ states. Similar effects are observed in the additional CD of ErTe$_3$ even though the features are broad and not resolved well. These additional CD features manifest the intrinsic CD effects in RTe$_3$ (R = Pr, Er) and consequently the chiral polarizations of the Te $5p$ bands despite their weak effects. Hence, these chiral polarizations of the Te $5p$ bands are expected to be related to the CDW formation in RTe$_3$. Meanwhile, only the overall geometrical CD effect is observed in PrTe$_2$, implying that the contribution from the chiral polarizations of Te $5p$ bands to the CDW formation in PrTe$_2$ is relatively weak.

The effect of linear dichroism (LD) in ARPES provides straightforward and very useful information on the symmetry of the orbital character. As shown in Figs. 8(a) and 8(b), the electric-field vector ($\vec{E}$) of the incident photons is always parallel to the sample surface in the linear-vertical (LV) polarization while, in the linear-horizontal (LH) polarization, $\vec{E}$ has both perpendicular and parallel components to the sample surface and has a significant amount of the perpendicular component when photons are incident at a glancing angle. Hence the stronger LH intensity reflects the out-of-plane orbital character (i.e., being perpendicular to the sample surface) while the stronger LV intensity reflects the in-plane orbital character (i.e., being parallel to the sample surface).

Figure 8 shows the effect of LD in ARPES of RTe$_n$. From left to right, Fig. 8(c) shows the ARPES image plots of PrTe$_2$ along $\bar{M}\bar{\Gamma}\bar{M}$, obtained with the LH and LV polarizations, and LD-ARPES (LD ≡ LH-LV). In LD-ARPES, red and blue represent the stronger LH and LV intensities, respectively. Similarly, Figs. 8(d) and 8(e) show the effect of LD in ARPES along $\bar{M}\bar{\Gamma}\bar{M}$ for PrTe$_3$ and ErTe$_3$, respectively.

Before discussing the LD effect in ARPES of RTe$_n$, we discuss the observed features in LH- and LV-ARPES bands of RTe$_n$ in Fig. 8. Many dispersive bands are observed clearly in ARPES. The large-energy-scale band structures are similar to one another in these three compounds, indicating that the measured ARPES bands represent the intrinsic features of RTe$_n$ and that these dispersive bands have the Te $5p$ character. In Fig. 8(f), the bands crossing through E_F at $\sim \pm \frac{1}{5}\Gamma M$ are observed, which are responsible for the FSs at the corresponding k_F values. The E_F-crossing bands are also observed in both PrTe$_3$ and ErTe$_3$. Indeed, the E_F-crossing positions in ErTe$_3$ agree very well with those in the calculated bands for the non-CDW phase of RTe$_n$ [see Fig. 8(h)], indicating that they have mainly Te $5p$ character and that the CDW deformation in RTe$_n$ is not so strong. This conclusion is supported by the good agreement between the measured and calculated band structures in ErTe$_3$, shown in Fig. 8(h). For reference, Fig. 8(g) shows the calculated band structures of ErTe$_3$ along several high-symmetry lines, obtained from the DFT calculations for the non-CDW phase (undistorted phase). Then good agreement is found in the comparison between the measured ARPES and the calculated band structures of ErTe$_3$ along $\bar{M}\bar{\Gamma}\bar{M}$ [see Fig. 8(h)].

Back to the discussion of the LD effect in RTe$_n$, first, the features in LD-ARPES are similar to one another. The dispersive bands between ~ -1 and ~ -3 eV exhibit the overall stronger LH polarization, indicating that these orbitals are

ordered mainly out of plane; i.e., they are ordered along the b axis perpendicular to the sample surface of the ac plane. In contrast, both the flat $R\,4f$ bands and the steeply dispersive bands, starting from these flat $R\,4f$ bands toward deep binding energies, exhibit the stronger LV polarization, indicating that these orbitals lie in the ac plane.

The region near E_F of the LD ARPES of PrTe$_2$ along $\bar{M}\bar{\Gamma}\bar{M}$ is shown in Fig. 8(f), where the E_F-crossing bands at $\sim \pm \frac{1}{5}\Gamma M$ exhibit the stronger LV polarization (blue). Therefore, these E_F-crossing bands are in-plane orbitals, as described above. In PrTe$_3$ and ErTe$_3$, the observed LD effects in the near-E_F states are not so clear as in PrTe$_2$. Nevertheless, the same conclusion can be made for PrTe$_3$ and ErTe$_3$ based on the overall similarity in three compounds. In conclusion, the E_F-crossing states in RTe$_n$, responsible for their CDW formations, originate mainly from the in-plane (ac plane)

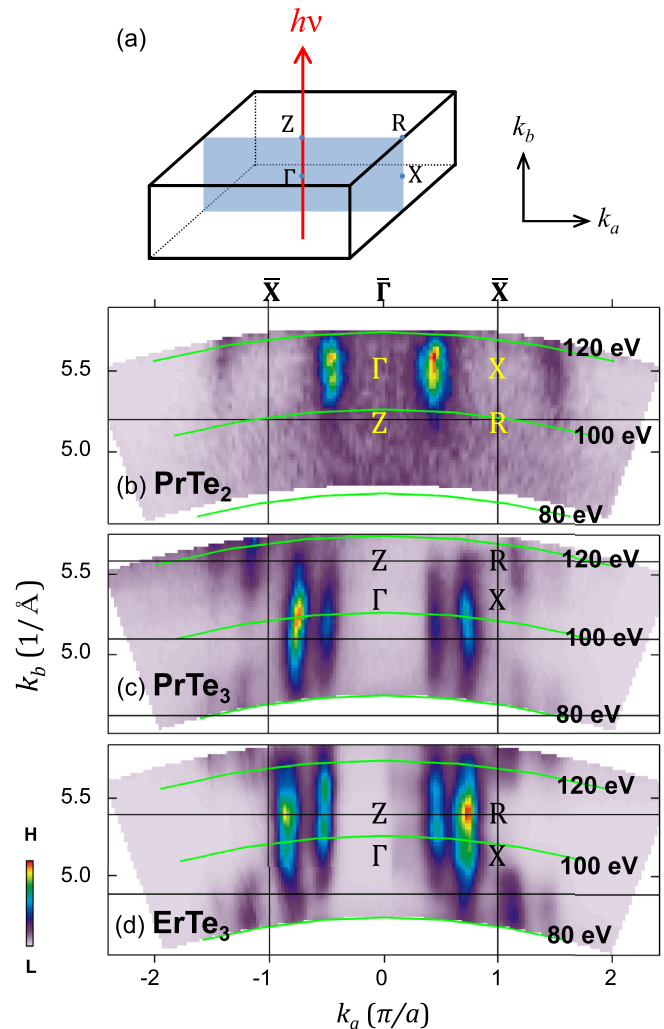FIG. 9. Photon energy ($h\nu$) maps of RTe$_n$ (R = Pr, Er; n = 2, 3). (a) The $h\nu$-map measurement was done on the plane (marked in blue) in the 3D BZ of RTe$_n$. (b) The Fermi-edge-state $h\nu$ map for PrTe$_2$, obtained for $h\nu$ in the range 80–120 eV. The horizontal and the vertical axes are along $k_{a(100)}$ and $k_{b(001)}$, respectively, where the variation in $h\nu$ is parallel to $k_{b(001)}$ ($\parallel h\nu$). [(c), (d)] Similarly for PrTe$_3$ and ErTe$_3$. These $h\nu$ maps cut through X-Γ-X (R-Z-R). All these $h\nu$ maps were obtained at T = 35 K.

orbitals of the Te sheets. This observation is consistent with the calculated band character of the E_F-crossing in-plane Te orbitals of Te sheets in $R\text{Te}_n$ [32].

VII. PHOTON ENERGY MAP

Figure 9 shows the measured $h\nu$ maps for the Fermi-edge states of $R\text{Te}_n$ (R = Pr, Er; n = 2, 3) in the range $80 \leqslant h\nu \leqslant \sim 120$ eV. The horizontal axis is parallel to $k_{a(100)}$ and the vertical axis is parallel to $k_{b(001)}$; i.e., the variation in $h\nu$ is $\parallel k_{b(001)}$. These $h\nu$ maps cut through X-Γ-X (also R-Z-R). In Fig. 9(a) is shown the plane of the $h\nu$ map measurement (blue) in the 3D BZ. In Figs. 9(b)–9(d) are shown the E_F-state $h\nu$ maps of PrTe_2, PrTe_3, and ErTe_3, respectively.

The major feature in the E_F-state $h\nu$ maps is the straight vertical dispersion along $h\nu \parallel k_b$ in all three compounds. Remember that the alternating R-Te(1) and Te(2)/Te(3) layers are stacked along the b axis (see Fig. 1). Hence, the straight vertical dispersions along k_b indicate that the near-E_F states have mainly 2D character, implying the weak interlayer interaction between R-Te(1) slabs and Te(2)/Te(3) sheets. Consequently, the effect of the interlayer interaction on the CDW formation would be very weak in $R\text{Te}_n$; i.e., the effect of the interlayer interaction on the near-E_F electronic states responsible for the CDW formation is weak.

VIII. SUMMARY AND PERSPECTIVE

The electronic structures of layered CDW compounds of PrTe_n (n = 2, 3) and ErTe_3 have been investigated via ARPES and XAS studies of high-quality stoichiometric single crystals. R $3d$ XAS measurements confirm the trivalent valency of R^{3+} ions, so that R-Te(1) slabs serve as charge reservoirs and the CDW instability occurs in the Te(2)/Te(3) sheets. R $4d \rightarrow 4f$ RPES study of PrTe_n (n = 2, 3) and ErTe_3 shows that the

R $4f$ states do not contribute directly to the CDW formation in $R\text{Te}_n$. Pr $4f$ electrons in PrTe_n, however, can contribute indirectly to the CDW distortion through the non-negligible Pr $4f$–Te $5p$ hybridization.

The twofold-symmetric features are observed in the CDW-induced FS of PrTe_3, arising from the putative 7×1 modulated structural formation. The origin of the distinct CDW deformations and single versus double CDW transitions in PrTe_3 and ErTe_3 is due to the larger lattice parameters of Te sheets and the resultant higher $N(E_F)$ in PrTe_3 than in ErTe_3. The higher T_{CDW} in PrTe_2 than in PrTe_3 originates from the higher Te $5p$-electron occupation and also the larger lattice parameters of Te sheets in PrTe_2 than in PrTe_3, both of which bring about the higher $N(E_F)$ and the concomitant higher T_{CDW}.

The intrinsic CD is observed in CDW-distorted $R\text{Te}_3$ (R = Pr, Er), indicating the $\vec{k}$-dependent chiral polarizations of the Te $5p$ bands, while only the geometrical CD is observed in PrTe_2, implying the relatively weak Te $5p$ chiral polarizations in PrTe_2. LD-ARPES confirms that the E_F-crossing orbitals are ordered in plane (i.e., in the ac plane) in PrTe_n (n = 2, 3) and ErTe_3. The near-E_F $h\nu$ maps exhibit the straight vertical dispersions along k_b, demonstrating the nearly 2D character for the near-E_F states and the weak interlayer coupling.

[1] N. W. Ashcroft and N. D. Mermin, *Solid State Physics* (Holt, Rinehart and Winston, New York, 1976).

[2] W. Kohn, Phys. Rev. Lett. **2**, 393 (1959).

[3] J. Voit, L. Perfetti, F. Zwick, H. Berger, G. Margaritondo, G. Grüner, H. Höchst, and M. Grioni, Science **290**, 501 (2000).

[4] T. Kasuya, M. H. Jung, and T. Takabatake, J. Magn. Magn. Mater. **220**, 235 (2000).

[5] H. Yao, J. A. Robertson, E. A. Kim, and S. A. Kivelson, Phys. Rev. B **74**, 245126 (2006).

[6] H. J. Kim, C. D. Malliakas, A. T. Tomić, S. H. Tessmer, M. G. Kanatzidis, and S. J. L. Billinge, Phys. Rev. Lett. **96**, 226401 (2006).

[7] N. Ru, C. L. Condron, G. Y. Margulis, K. Y. Shin, J. Laverock, S. B. Dugdale, M. F. Toney, and I. R. Fisher, Phys. Rev. B **77**, 035114 (2008).

[8] A. Fang, N. Ru, I. R. Fisher, and A. Kapitulnik, Phys. Rev. Lett. **99**, 046401 (2007).

[9] K. Yumigeta, Y. Qin, H. Li, M. Blei, Y. Attarde, C. Kopas, and S. Tongay, Adv. Sci. **8**, 2004762 (2021).

[10] Note that the symmetry points of the orthorhombic BZ are assigned differently from the ones in Fig. 1(e). We consider, for PrTe_3, X and M of nearly square-type Γ-centered BZ (due to $a \approx c$), just for the comparison with those for PrTe_2.

[11] M. Grioni, I. Vobomik, F. Zwick, and G. Margaritondo, J. Electron Spectrosc. Relat. Phenom. **100**, 313 (1999).

[12] P. Aebi, T. Pillo, H. Berger, and F. Levy, J. Electron Spectrosc. Relat. Phenom. **117-118**, 433 (2001).

[13] S. V. Borisenko, A. A. Kordyuk, A. N. Yaresko, V. B. Zabolotnyy, D. S. Inosov, R. Schuster, B. Büchner, R. Weber, R. Follath, and L. Patthey, and H. Berger, Phys. Rev. Lett. **100**, 196402 (2008).

[14] K. Rossnagel, J. Phys.: Condens. Matter **23**, 213001 (2011).

[15] R. G. Moore, V. Brouet, R. He, D. H. Lu, N. Ru, J.-H. Chu, I. R. Fisher, and Z.-X. Shen, Phys. Rev. B **81**, 073102 (2010).

[16] N. Lazarevic, Z. V. Popovic, Rongwei Hu, and C. Petrovic, Phys. Rev. B **83**, 024302 (2011).

[17] H.-M. Eiter, M. Lavagnini, R. Hackl, E. A. Nowadnick, A. F. Kemper, T. P. Devereaux, J.-H. Chu, J. A. Analytis, I. R. Fisher, and L. Degiorgi, Proc. Natl. Acad. Sci. USA **110**, 64 (2013).

[18] A. Kikuchi, J. Phys. Soc. Jpn. **67**, 1308 (1998).

[19] K. Stöwe, J. Alloys Compd. **307**, 101 (2000); J. Solid State Chem. **149**, 155 (2000).

[20] G.-H. Gweon, J. D. Denlinger, J. A. Clack, J. W. Allen, C. G. Olson, E. D. DiMasi, M. C. Aronson, B. Foran, and S. Lee, Phys. Rev. Lett. **81**, 886 (1998).

[21] H. Komoda, T. Sato, S. Souma, T. Takahashi, Y. Ito, and K. Suzuki, Phys. Rev. B **70**, 195101 (2004).

[22] J. Laverock, S. B. Dugdale, Z. Major, M. A. Alam, N. Ru, I. R. Fisher, G. Santi, and E. Bruno, Phys. Rev. B **71**, 085114 (2005).

[23] V. Brouet, W. L. Yang, X. J. Zhou, Z. Hussain, R. G. Moore, R. He, D. H. Lu, Z. X. Shen, J. Laverock, S. B. Dugdale, N. Ru, and I. R. Fisher, Phys. Rev. B **77**, 235104 (2008), and references therein.

[24] E. Lee, D. H. Kim, H. W. Kim, J. D. Denlinger, H. Kim, J. Kim, K. Kim, B. I. Min, B. H. Min, Y. S. Kwon, and J.-S. Kang, Sci. Rep. **6**, 30318 (2016).

[25] S. Seong, H. Kim, K. Kim, B. I. Min, Y. S. Kwon, S. W. Han, B.-G. Park, R. Stania, Y. Seo, and J.-S. Kang, Phys. Rev. B **104**, 195153 (2021).

[26] K. Y. Shin, V. Brouet, N. Ru, Z. X. Shen, and I. R. Fisher, Phys. Rev. B **72**, 085132 (2005).

[27] J.-S. Kang, C. G. Olson, Y. S. Kwon, J. H. Shim, and B. I. Min, Phys. Rev. B **74**, 085115 (2006).

[28] D. R. Garcia, G.-H. Gweon, S. Y. Zhou, J. Graf, C. M. Jozwiak, M. H. Jung, Y. S. Kwon, and A. Lanzara, Phys. Rev. Lett. **98**, 166403 (2007).

[29] M. Lavagnini, M. Baldini, A. Sacchetti, D. Di Castro, B. Delley, R. Monnier, J.-H. Chu, N. Ru, I. R. Fisher, P. Postorino, and L. Degiorgi, Phys. Rev. B **78**, 201101(R) (2008).

[30] M. Maschek, S. Rosenkranz, R. Heid, A. H. Said, P. Giraldo-Gallo, I. R. Fisher, and F. Weber, Phys. Rev. B **91**, 235146 (2015).

[31] M. Maschek, D. A. Zocco, S. Rosenkranz, R. Heid, A. H. Said, A. Alatas, P. Walmsley, I. R. Fisher, and F. Weber, Phys. Rev. B **98**, 094304 (2018).

[32] E. Lee, D. H. Kim, J. D. Denlinger, J. Kim, K. Kim, B. I. Min, B. H. Min, Y. S. Kwon, and J.-S. Kang, Phys. Rev. B **91**, 125137 (2015).

[33] P. Li, B. Lv, Y. Fang, W. Guo, Z. Wu, Y. Wu, D. Shen, Y. Nie, L. Petaccia, C. Cao, and Z. A. Xu, and Y. Liu, Sci. China Phys. Mech. Astron. **64**, 237412 (2021).

[34] N. Ru, Ph.D. thesis, Stanford University, 2008.

[35] M. H. Jung, A. Alsmadi, H. C. Kim, Y. Bang, K. H. Ahn, K. Umeo, A. H. Lacerda, H. Nakotte, H. C. Ri, and T. Takabatake, Phys. Rev. B **67**, 212504 (2003).

[36] Y. S. Kwon and B. H. Min, Phys. B: Condens. Matter **281-282**, 120 (2000).

[37] C. Malliakas, S. J. L. Billinge, H. J. Kim, and M. G. Kanatzidis, J. Am. Chem. Soc. **127**, 6510 (2005).

[38] J. A. W. Straquadine, F. Weber, S. Rosenkranz, A. H. Said, and I. R. Fisher, Phys. Rev. B **99**, 235138 (2019).

[39] J. Gjerde and R. Jishi, Crystals **12**, 1839 (2022).

[40] M. Lavagnini, Ph.D. thesis, Swiss Federal Institute of Technology, Zurich, 2009.

[41] J. W. Allen, S.-J. Oh, O. Gunnarsson, K. Schönhammer, M. B. Maple, M. S. Torikachvili, and I. Lindau, Adv. Phys. **35**, 275 (1986).

[42] P. A. Cox, Y. Baer, and C. K. Jørgesen, Chem. Phys. Lett. **22**, 433 (1973); P. A. Cox, *Structure and Bonding*, Photoelectron Spectrometry, Vol. 24 (Springer, New York, 1975), p. 59.

[43] F. Gerken, A. S. Flodstrom, J. Barth, L. I. Johnsson, and C. Kunz, Phys. Scr. **32**, 43 (1985).

[44] O. Gunnarsson and K. Schönhammer, Phys. Rev. B **28**, 4315 (1983); **31**, 4815 (1985); *Handbook on the Physics and Chemistry of Rare Earths*, edited by K. A. Gschneidner, L. Eyring, and S. Hüfner (North Holland, Amsterdam, 1987), Vol. 10, p. 103.

[45] B. I. Min, H. J. F. Jansen, T. Oguchi, and A. J. Freeman, Phys. Rev. B **33**, 8005 (1986).

[46] H. Kim, J. Kim, and B. I. Min, DFT calculations (unpublished).

[47] A. Tomic, Z. Rak, J. P. Veazey, C. D. Malliakas, S. D. Mahanti, M. G. Kanatzidis, and S. H. Tessmer, Phys. Rev. B **79**, 085422 (2009).

[48] A. Kot, K. Placheta, M. Radecka, and K. Zakrzewska, International School and Symposium on Synchrotron Radiation in Natural Science, Krakow, Poland, 22-25 August 2022 (unpublished).

[49] J. K. Burdett and S. Lee, J. Am. Chem. Soc. **105**, 1079 (1983).

[50] G. A. Papoian and R. Hoffmann, Angew. Chem. Int. Ed. **39**, 2408 (2000).

[51] E. DiMasi, B. Foran, M. C. Aronson, and S. Lee, Phys. Rev. B **54**, 13587 (1996).

[52] J. H. Shim, J.-S. Kang, and B. I. Min, Phys. Rev. Lett. **93**, 156406 (2004).

[53] J.-S. Kang, D. H. Kim, H. J. Lee, J. Hwang, H.-K. Lee, H.-D. Kim, B. H. Min, K. E. Lee, Y. S. Kwon, J. W. Kim, Kyoo Kim, B. H. Kim, and B. I. Min, Phys. Rev. B **85**, 085104 (2012).

[54] In fact, the bilayer splitting, predicted in the calculated CE maps, is not resolved well in the measured CE maps. However, the separation of the predicted small bilayer splitting is within the width of the measured CE data. So we think that this discrepancy does not conflict with the good agreement between experiment and calculations.

[55] R. G. Moore, W. S. Lee, P. S. Kirchman, Y. D. Chuang, A. F. Kemper, M. Trigo, L. Patthey, D. H. Lu, O. Krupin, M. Yi, D. A. Reis, D. Doering, P. Denes, W. F. Schlotter, J. J. Turner, G. Hays, P. Hering, T. Benson, J.-H. Chu, T. P. Devereaux, I. R. Fisher, Z. Hussain, and Z.-X. Shen, Phys. Rev. B **93**, 024304 (2016).

[56] Y. A. Bychkov and E. I. Rashba, JETP Lett. **39**, 78 (1984).

[57] A. Kaminski, S. Rosenkranz, H. M. Fretwell, J. C. Campuzano, Z. Li, H. Raffy, W. G. Cullen, H. You, C. G. Olson, C. M. Varma, and H. Höchst, Nature (London) **416**, 610 (2002).

[58] S. Cho, J.-H. Park, J. Hong, J. Jung, B. S. Kim, G. Han, W. Kyung, Y. Kim, S.-K. Mo, J. D. Denlinger, J. H. Shim, J. H. Han, C. Kim, and S. R. Park, Phys. Rev. Lett. **121**, 186401 (2018).

[59] No CD FS map data for $PrTe_2$ are presented in this paper because we have not measured CD FS maps for $PrTe_2$.